A cluster-based pore network model of drying with corner liquid films with application to a macroporous material

Sreejuth Lal, Marc Prat, Mathieu Plamondon, Lily Poulikakos, Manfred N. Partl, Dominique Derome, Jan Carmeliet

A cluster-based pore network model of drying with corner liquid films, with application to a macroporous material

Sreeyuth Lal [a,b,*], Marc Prat [c], Mathieu Plamondon [d], Lily Poulikakos [e], Manfred N. Partl [e], Dominique Derome [a], Jan Carmeliet [f]

[a] Laboratory for Multiscale Studies in Building Physics, Empa, Überlandstrasse 129, CH-8600 Dübendorf, Switzerland
[b] Department of Civil, Environmental and Geomatic Engineering, ETH Zurich, CH-8093 Zurich, Switzerland
[c] Institut de Mécanique des Fluides de Toulouse (IMFT), Université de Toulouse, CNRS, Toulouse, France
[d] Reliability Science and Technology Laboratory, Empa, Überlandstrasse 129, CH-8600 Dübendorf, Switzerland
[e] Road Engineering/Sealing Components Laboratory, Empa, Überlandstrasse 129, CH-8600 Dübendorf, Switzerland
[f] Chair of Building Physics, ETH Zürich, CH-8093 Zurich, Switzerland

Keywords:
Pore network modeling
Macroporous media
Drying
Porous asphalt

A B S T R A C T

A pore network model (PNM) of drying in a gravity dominated macroporous material has been developed. The pore network geometry used for the simulations is extracted from microcomputed tomography scans of porous asphalt (PA), a macroporous, hydrophobic material. The drying of liquid water in PA is modeled using a cluster based approach with a two step drying process i.e. elements go first from being fully saturated to having liquid only in pore and throat corners, and then to becoming completely dry. The PNM simulations are validated with gravimetric experiments performed under controlled conditions and the simulations show good agreement with experiments for most of the drying period. From experiments, it is seen that drying in PA completely skips the constant drying rate period (CDRP) and instead begins with the decreasing drying rate period (DDRP) due to the poor hydraulic connectivity in PA as a result of its large and hydrophobic pore space. The PNM simulations exhibit CDRP initially and then transitions to DDRP after a third of the total drying time. The CDRP at the beginning of the PNM simulations is due to the simplified liquid configuration assumed in the network, and its duration can be minimized to an extent by increasing the number of hydrophobic pores in the network that does not retain any liquid after drainage. Although promising, the first results call for a more accurate representation of both the complex pore space of PA and the physics involved in drying of a macroporous material.

1. Introduction

The durability of several porous materials that are constantly exposed to the environment such as concrete, sandstone, limestone, brick, asphalt, etc. is directly proportional to the residence time of water within these materials as water is one of the main agents of their degradation. Evaporative drying is one of the most important factors that determine the residence time of water in such porous media. In a macroporous material (defined here as a material with pore sizes larger than 0.1 mm) with a highly complex pore space, drying is influenced by several pore scale mechanisms as well as by the matrix material characteristics. If the solid matrix of the porous medium is hydrophobic, the resulting low connectivity of the liquid phase during drying leads to a high capillary number drying regime, in which the mass transfer is dominated by vapor diffusion both within and near the external surface of the medium that is exposed to the environment [1,2]. The modeling of such a drying regime using simplified models presents an interesting case.

Porous asphalt (PA), a macroporous medium with pore sizes ranging from micrometers to millimeters, is a material whose durability is particularly sensitive to the residence time of water within the structure. PA is used as the surface layer of roads for enhanced seepage of water, thereby preventing aquaplaning and splash spray effects during and after rain events. PA has a porosity of 15–20% and is a composite material made from fine and coarse mineral aggregates, a bituminous binder and air voids. Due to its high permeability, a large area of the internal structure of PA is exposed to water during a rain event. Although most of the water within PA drains due to gravity, some residual water remains as corner films in hydrophilic pores and as bulk liquid in dead end

* Corresponding author at: RWDI Inc, Guelph, ON, Canada.
E-mail address: Sreeyuth.lal@rwdi.com (S. Lal).

pores, as observed in previous experiments [3 5]. The drying of this residual liquid content is influenced by various conditions such as airflow (where air speed [6], relative humidity [7] and air temperature are the influencing main parameters), solar radiation and vehicular loads. However, radiative drying is not considered in this study as the enhanced complexity of modeling non isothermal drying by including solar radiation as an input factor is not justifi able since water retention in PA is a serious concern only in cold and wet conditions i.e. when radiative drying is not very promi nent. An additional justification for assuming isothermal drying is that previous experiments have shown that phase change does not cool the material significantly [3 5]. Therefore, the focus of this study is on modeling isothermal, convective drying of liquid water in PA in a controlled environment, using pore network modeling (PNM).

Pore network modeling (PNM) is based on the representation of the void space in a material as a network of wide pores connected to each other by narrow throats. Multiphase flow in porous media was first represented using pore networks by Fatt [8]. Since then, several researchers have used PNM to study various flow mecha nisms such as drainage [9 11], imbibition [12 14] and drying [2,15 20]. In PNM, essentially pore scale equations are solved in the given domain of pores and throats. PNM was used to model drying for the first time by Prat [21]. His model combined the prin ciples of invasion percolation with a discrete computation of diffu sive vapor transport in the medium. Moreover, Prat [21] was the first to use pore networks to investigate liquid patterns during the drying process and assess its influence on the drying rates. Prat [21] applied invasion percolation (IP) to drying by drawing an anal ogy between the drying and drainage processes as both are charac terized by the movement of menisci through the porous medium and the progressive invasion of the non wetting fluid. This analogy was first drawn by Shaw [22] who experimentally observed the similarity of drying invasion fronts to drainage invasion fronts. Subsequent studies [23,24] reinforced this analogy, specifically by observing that viscous effects stabilize invasion. The key differ ence, however, between the different IP algorithms of drainage and drying is the treatment of the disconnected liquid clusters. In case of a wet throat in such a cluster, even if the drainage stops, drying continues to take place and this should be incorporated into the IP algorithm for a realistic simulation, as shown by the model and validation experiments on etched networks by Laurindo & Prat [15]. However, when viscous effects in the gas and liquid phase are considered, the drying behavior departs from an invasion per colation process [23].

Since Prat [21], increasingly sophisticated IP algorithms have been proposed to take into account gravity effects [25], thermal effects [26], viscous effects [27] and the presence of an external mass transfer boundary layer [28]. A common feature of most of the earlier studies, however, is the absence of consideration of liq uid films during the drying process. The presence of liquid films in pore and throat corners influences drying in multiple ways. On the one hand, films increase the hydraulic connectivity of the liquid phase and provide a pathway for liquid drainage. On the other hand, the gas phase within pores containing films remains near saturated, thereby drastically slowing down the evaporation in such pores. Experiments by Vorhauer et al. [29] have also indicated the role of liquid films in accelerating drying in a model porous medium. Yiotis et al. [30] was the first to consider the effect of films when modeling isothermal drying using pore networks. As expected, the spread of films increased with a decrease in capillary number, which is the ratio of viscous to capillary force. However, the effect of gravity was not considered in their model. Yiotis et al. [31] determined the extent of the film region in the porous domain as a function of the particle size distribution of the porous medium. When gravity plays an increasing role, the growth of the film region as the percolation front moves away from the surface becomes less pronounced due to earlier film detachment from the percolation inlet surface. Additionally, with the increasing influence of gravity, the constant drying rate period (CDRP) became shorter as a result of the smaller film regions and the decreasing drying rate period (DDRP) set in earlier. Yiotis et al. [2] showed that, as the Bond number increased, i.e. as the relative influence of gravity compared to surface tension forces increased, the film thickness profiles, and therefore the capillary pressure gradients in the system, also became more complex, a situation which leads to shorter film regions and shorter CDRPs. However, the pore sizes of the porous medium considered in the presented study are much larger than those studied in Yiotis et al. [2], and therefore, the dry ing regimes and drying behavior investigated in this study are expected to be different from those in their study.

The main objective of this study is to model with PNM the dry ing of liquid water in a macroporous, hydrophobic medium, using a cluster based, sequential algorithm with consideration of the pos sible presence of corner liquid films. The results, in particular the drying rate, of the proposed drying model are compared to those from gravimetric experiments under controlled conditions. Sensi tivity analyses are also performed to analyze the influence of cor ner films on the proposed drying model.

It must be emphasized that the modeling of corner liquid films in the present work is markedly different from previous works [30 33]. In those works, the viscous flow in the films is explicitly computed but not the possible transport between clusters of liquid saturated pores via the films (this is because the boundary condition between the films and the liquid clusters for the film flow problem is the same on every liquid cluster). By contrast, in the present effort, the emphasis is on the possible hydraulic inter connectivity between clusters. However, viscous flow within the liquid films is not explicitly computed assuming that capillarity and gravity (in the initial stage) controls the pore invasion every where, i.e. both in pores (or throats) containing a bulk meniscus and pores (or throats) containing film menisci. Thus, here, the role of the films is essentially to maintain the hydraulic connectivity between saturated pore clusters. For example, two separated groups of liquid saturated pores connected by liquid films are con sidered as a single liquid cluster in our model whereas they are considered as two distinct clusters in [30 33]. Also, in these works, the liquid stored in films is not explicitly tracked as the liquid mass in films is considered negligible compared to the overall initial liq uid mass. In the drying model developed in this study, the liquid mass in the films is explicitly tracked.

2. Pore network modeling

2.1. Pore network with corner films

A pore network consists of representing the larger pores in the medium as a set of nodes, and the smaller pores connecting these larger pores as a set of links or throats. Typically, a pore network is extracted from three dimensional scans of materials after the seg mentation of the pore space using techniques such as skeletoniza tion [34] and watershed method [35]. Physical properties such as volume, conductance etc. are then applied to these elements i.e. pores and throats. In Fig. 1, the representation of an irregular pore space with triangular pores and throats is shown. Although various geometrical shapes are used to represent irregular pore space, a traingular cross section is used in this study, the justification for and details of which are given in Section 3. In pore network mod eling, transport equations are solved at pore centers. As a result, the diffusion length within pores is equal to its inscribed radius r_0 while the diffusion length within throats is equal to the distance

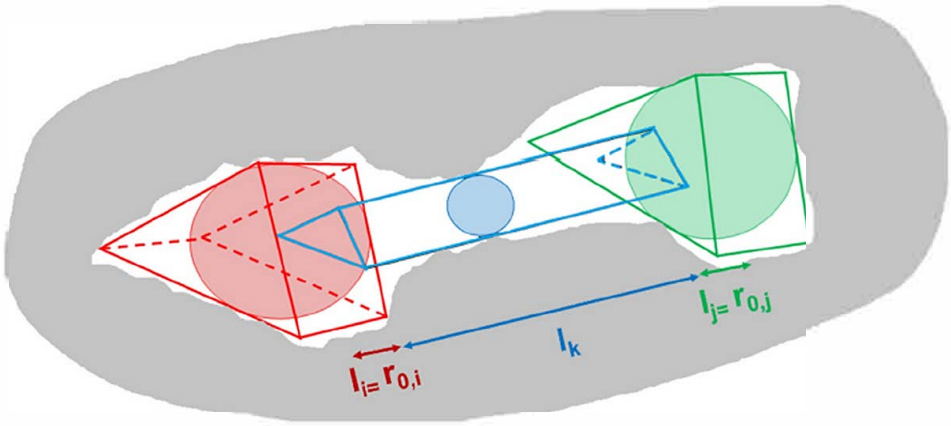

Fig. 1. Schematic representation of an irregular pore space (white) using triangular pores (red, green) and a triangular throat (blue). First, the pores i and j and throat k are represented with the largest circle that can be fitted inside them. A circumscribed equilateral triangle is then fitted around the circle. In case of a pore, the radius of the inscribed circle (r_0) is also the pore diffusion length, while in case of a throat, the diameter of the inscribed circle is the throat width and the distance between the two pore surfaces is the throat length. The total diffusion length of this pore system is therefore $r_{0,i} + r_{0,j} + l_k$. (For interpretation of the references to colour in this figure legend, the reader is referred to the web version of this article.)

between the two pore surfaces connected to it. The total diffusion length between two pores is therefore the sum of their radii and the distance between their surfaces, as shown in Fig. 1.

Many studies have shown that the pore shapes of actual porous media are highly irregular and non circular and that during two phase flow, the wetting phase occupies the pore corners while the non wetting phase occupies the pore center, as shown schematically in Fig. 2 for a triangular pore. The films of wetting fluid formed at pore corners are referred to as arc menisci (AMs). The radius of curvature of an arc meniscus, r_{nw}, is also shown in Fig. 2.

In this study, as described in detail in the next section, drying in PA is simulated through a pore network model of water vapor dif fusion from the evaporating front of water filled pores to the envi ronment, through an air boundary layer thickness. Once the PA pore space is defined and the liquid distribution at a given stage of drying is determined, vapor flow rate through the network is computed by defining a vapor conductance, $g_{v,e}$ [m s], in all dry elements (e) i.e. elements with no liquid content:

$$g_{v,e} \quad \frac{D_{va}A_e}{l_e R_v T} \tag{1}$$

where D_{va} 2.068×10^{-5} m^2 s^{-1} is the binary diffusion coefficient of water vapor through dry air, A_e[m^2] is the element cross section area, l_e[m]is the element length, R_v 461.524 J kg^{-1} K^{-1} is the specific gas constant of water vapor and T [K] is the temperature. Note that an element can either be a pore or a throat. The vapor conductance in liquid filled elements is zero. Once the vapor con ductances of all dry elements are determined, the throat conduc tances, which are used for the network transport calculations, are defined as the harmonic mean of the local conductance of the throat itself and of the two pores connected to it. For instance, for the con figuration shown in Fig. 1, the total vapor conductance of the sys tem of pores and throats is defined as:

$$g_{v,ijk} \quad \frac{1}{\frac{1}{g_{v,i}} + \frac{1}{g_{v,j}} + \frac{1}{g_{v,k}}}; \tag{2}$$

where $g_{v,i}$, $g_{v,j}$ and $g_{v,k}$ are the local vapor conductances of the two pores and the throat connecting them, respectively. Thereafter, the local vapor partial pressure of all pores in the network are calcu lated by solving a linear system of equations resulting from the imposition of mass conservation condition at all pores i.e. the fluxes entering a pore are equal to the fluxes leaving the pore. For the pore system shown in Fig. 1, the vapor flux, q_v [kg s^{-1}] between the two pores is calculated as:

$$q_{v,ii} \quad g_{v,iik}(p_{v,i} \quad p_{v,i}). \tag{3}$$

where $p_{v,i}$ and $p_{v,j}$ are the local vapor partial pressures at the two pores. When the local vapor partial pressure of each pore is known, the vapor flux leaving the entire network can be determined as:

$$q_{v,out} \quad \sum g_{v,out\ i}(p_{v,\infty} \quad p_{v,out\ i}) \tag{4}$$

where the subscript out i represents the elements that are at the outlet boundary and $p_{v,\infty}$ is the environmental vapor partial pressure.

After calculating the outlet vapor flux at each step, the water distribution within the network is adjusted according to the algo rithm described in the next section. In general, in an element with two phase distribution i.e. liquid water in the corners and the remaining part filled with vapor, the cross sectional area of the wetting phase (liquid water in this study) is given by:

$$A_w \quad N_c r_{nw}^2 \left[\frac{\cos\theta}{\sin\alpha_c} \cos(\alpha_c + \theta) \quad \frac{\pi}{2} + \alpha_c + \theta \right] \tag{5}$$

where N_c is the number of corners, r_{nw} $\frac{\gamma}{p_c^c}$ is the radius of the arc menisci (AMs) in the corner where γ [N/m] is the air water surface tension and p_c^c is the threshold pressure (see Section 2.2), θ is the

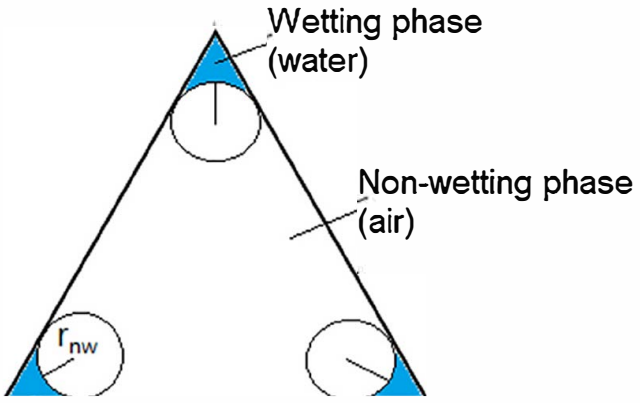

Fig. 2. Schematic representation of arc menisci in an equilateral triangle during two-phase flow in an angular geometry. The radius of curvature of an arc meniscus r_{nw} is also given. The filled corners are referred to as films.

receding contact angle and α_c is the corner half angle. A receding contact angle is used since drying in PA occurs with a receding front. Note that Eq. (5) is valid for polygonal regular cross section of N_c equal segments and equal corner angles [36,37]. The cross sectional area occupied by the non wetting phase (air in this study) is:

$$A_{nw} \quad A_{tot} \quad A_w \quad 3\sqrt{3}r_0^2 \quad A_w, \tag{6}$$

where A_{tot} is the total cross section area and r_0 is the inscribed radius of the element. In the simulations in this study, an upper limit for the AM radius, r_{nw}^t, is imposed according to Wong et al. [38]:

$$r_{nw}^t \quad \frac{r_0}{\chi}. \tag{7}$$

According to Mason & Morrow [39], the dimensionless curva ture, χ, can be expressed as a function of the static contact angle, θ, and the critical contact angle, $\theta_c \quad \frac{\pi}{N_c}$, as:

$$\chi \quad cos\theta + \left[\frac{(\theta_c \quad \theta + sin\theta cos\theta)}{tan\theta_c}\right]^{\frac{1}{2}}. \tag{8}$$

Note that the critical contact angle is the angle below which the formation of arc menisci takes place.

2.2. Cluster based drying model

In a previous study [4], it has been observed that, when fully saturated PA specimens are subjected to drainage and drying, the time scale of the two processes are clearly distinct. While gravity driven drainage in PA is a fast process in the order of sec onds, the subsequent drying process can take hours or days, depending upon the specimen size and environmental conditions. However, knowledge about the exact liquid distribution in PA specimens at the end of drainage and, therefore at the onset of evaporative drying, is still an open question due to the limitations of imaging thin liquid films in a solid matrix with a hydrogenous component like bitumen. Therefore, in this study, an initial two phase (air and water) distribution is assumed in the network at the beginning of drying, based on the results from previous studies [3 5].

Depending upon the fluid configuration within each element, elements are defined as a 'dry' element, a 'film' element or a 'bulk element'. If an element is already invaded by air, liquid is present at its corners as arc menisci, and such an element is referred to as a film element. Elements in which water occupies the entire cross section, although they may or may not be fully liquid satu rated, are referred to as bulk elements. Thus, the volume of liquid, V_{lt}, in a wet (film or bulk) element is defined as:

$$V_{lt} \quad \begin{cases} V_{lb} + V_{lf}, & \text{for bulk elements} \\ V_{lf}, & \text{for film elements,} \end{cases} \tag{9}$$

where V_{lb} is the volume of liquid in the center (bulk) of the element and V_{lf} is the volume of liquid in the corner films (AMs). On the other hand, a 'dry' element, as the name implies, is assumed to be fully saturated with air i.e. there is no liquid water or water vapor. Drying is assumed to take place only at the top surface of the net work, where a convective mass transfer boundary condition is applied by specifying the evaporation flux density [33], $e\left[\text{kg m}^{-2}\text{ s}^{-1}\right]$:

$$e \quad \rho_g D_{va} \frac{(c_{out\ i} \quad c_\infty)}{\delta}, \tag{10}$$

where ρ_g $\left[\text{kg m}^{-3}\right]$ is the gas phase density, $c_{out\ i}[\ ]$ and c_∞ $[\ ]$ are the water vapor mass fractions at the top surface pores and the environment respectively, and δ $[m]$ is the air boundary layer thick ness across which the transfer of vapor from the open surface of the porous medium to the environment takes place. In other words, the convective mass transfer boundary condition is imposed by specify ing the throat length, $l_t \quad \delta$, for the all throats near the open surface.

The film thickness in the film elements at the beginning of dry ing is determined using the Mayer and Stowe [40] and Princen [41] (MS P) method, which equates the radius of curvature of AMs to the curvature of the invading air water interface. As discussed in Lal et al. [5], the Bond number of PA11 is approximately 6. Bond number is a dimensionless number representing the competition between capillary and gravity forces, and a Bond number larger than 1 indicates the dominance of gravity. Therefore, the MS P method is extended here to include the effect of gravity, g, as an additional term of pressure difference. The values of all parameters in the equations below are given in the discussion section. The threshold capillary pressure, p_c^t, according to the MS P method, with the addition of the effect of the gravity, is:

$$p_c^t \quad \left(\frac{\gamma}{r_0} cos\theta_r \left(1 + 2\sqrt{\pi G}\right) F_d(\theta_r, G)\right) \quad \rho_l g \Delta h, \tag{11a}$$

$$F_d(\theta_r, G) \quad \frac{1 + \sqrt{1 + \frac{4GY}{cos^2\theta_r}}}{1 + 2\sqrt{\pi G}}, \tag{11b}$$

$$Y \quad \pi\left(1 \quad \frac{\theta_r}{60}\right) + 3sin\theta_r cos\theta_r \quad \frac{cos^2\theta_r}{4G}. \tag{11c}$$

where θ_r is the receding contact angle, G $[\ ]$ is the shape factor of the pore, $\rho_l[\text{kg m}^{-3}]$ is the liquid phase density, and Δh is the posi tion of the pore or throat with respect to the lowest point in the cluster to which it belongs. If AMs are assumed to be present at all corners, the function $F_d(\theta_r, G)$ is universal for a given G and Y is only dependent on θ_r. The equations given above are based on the principle that, if AMs are displaced by a small distance, the work for the displacement is balanced by the change in surface free energy. A detailed derivation of the expressions in Eq. (11) is given by Oren et al. [42]. At the beginning of drying, all film elements have a film thickness corresponding to the threshold pressure (Eq. (11a)) of the largest interfacial bulk throat in the network (it is assumed that initially all the liquid clusters are interconnected via the films).

In a highly complex pore space such as that of PA, the formation of clusters of liquid and gas regions is expected during the drying process. Therefore, the next step is to model the drying of this residual liquid content with a cluster based drying algorithm, in which the following assumptions are made:

1. The vapor mass fraction in a pore adjacent to a throat contain ing liquid is the saturation vapor mass fraction, c_e.
2. Since liquid regions are assumed to be hydraulically connected, capillary equilibrium is assumed. This means that the corner film radii are equal in all the elements that are part of the same cluster.
3. An element is assumed to be dry when the corner film radius becomes lower than a threshold value, $r_{0nw,min}$, where $\eta \ll 1$.
4. Viscous effects are neglected.
5. The drying is isothermal.

The drying algorithm developed in this study is similar to that in Prat [21] but with the additional consideration of film elements. In essence, drying proceeds by first drying the central area of bulk elements and then proceeds to dry the film elements by decreasing their liquid film thickness in a step by step manner. Since viscous effects in saturated pores and throats are neglected, invasion per colation rules can be applied to determine the element that is invaded in every step in each cluster [21]. Note that viscous effects

are also neglected in the films. Thus, the model is fully consistent only for very low evaporation rates for which the extent of the films is marginally limited by the viscous effects. The PNM simulations in this study are performed with custom modules developed within the framework of the open source pore network modeling code OpenPNM [43], which is written in Python with Scipy.

The flowchart of the drying algorithm developed in this study is given in Fig. 3 while the detailed algorithm is as follows:

1. Identify all liquid clusters *cl* present in the network.
2. Determine the radius of the largest element in each cluster *i*, $r^i_{0max,cl}$. If the cluster contains bulk elements, $r^i_{0max,cl}$ is determined considering only the bulk elements. In other words, the film elements are not considered for determining $r^i_{0max,cl}$ in this case.
3. Compute the vapor mass fraction field in all the fully dry pores in the network.
4. Compute evaporation rate F^i_{cl} [kg/s] at the boundary of each liquid cluster present in the network by computing the vapor flow through the elements adjacent to the cluster boundary elements (Eq. (3)).
5. Determine the evaporation time to either fully dry or dry the center of the element (excluding the corner films) with the maximum size in each cluster as follows. If a cluster *i* contains one or more bulk elements, then t^i_{cl} $\frac{\rho_l V_{lb}}{F^i_{cl}}$, where V_{lb} is the volume of liquid in the center of the element determined in step #2. Note that a bulk throat becomes a film throat when the liquid goes from occupying the entire cross section to becoming films with a radius of $\frac{r_t}{\chi}$. If a cluster *i* contains only film elements, the procedure is as follows. Suppose the corner film radius of curvature is $r^i_{nw,cl}(t)$ in the considered cluster at time *t*. Then the volume of liquid V^k_{lf} in each element *k* of this cluster can be computed from $r^i_{nw,cl}(t)$ (Eq. (5)). From this, the mass of liquid present in this cluster can be computed as m^i_{cl} $\rho_l \sum_k^{n_k} {}_1 V^k_{lf}$. The evaporation time to fully dry the largest element in the cluster will therefore be t^i_{cl} $\frac{\left(m^i_{cl}\left(r^i_{nw,cl}(t)\right) - m^i_{cl}\left(\eta r^i_{0max,cl}\right)\right)}{F^i_{cl}}$, where $\eta r^i_{0max,cl}$ is the radius at which the largest element in the cluster is assumed to be fully dry.

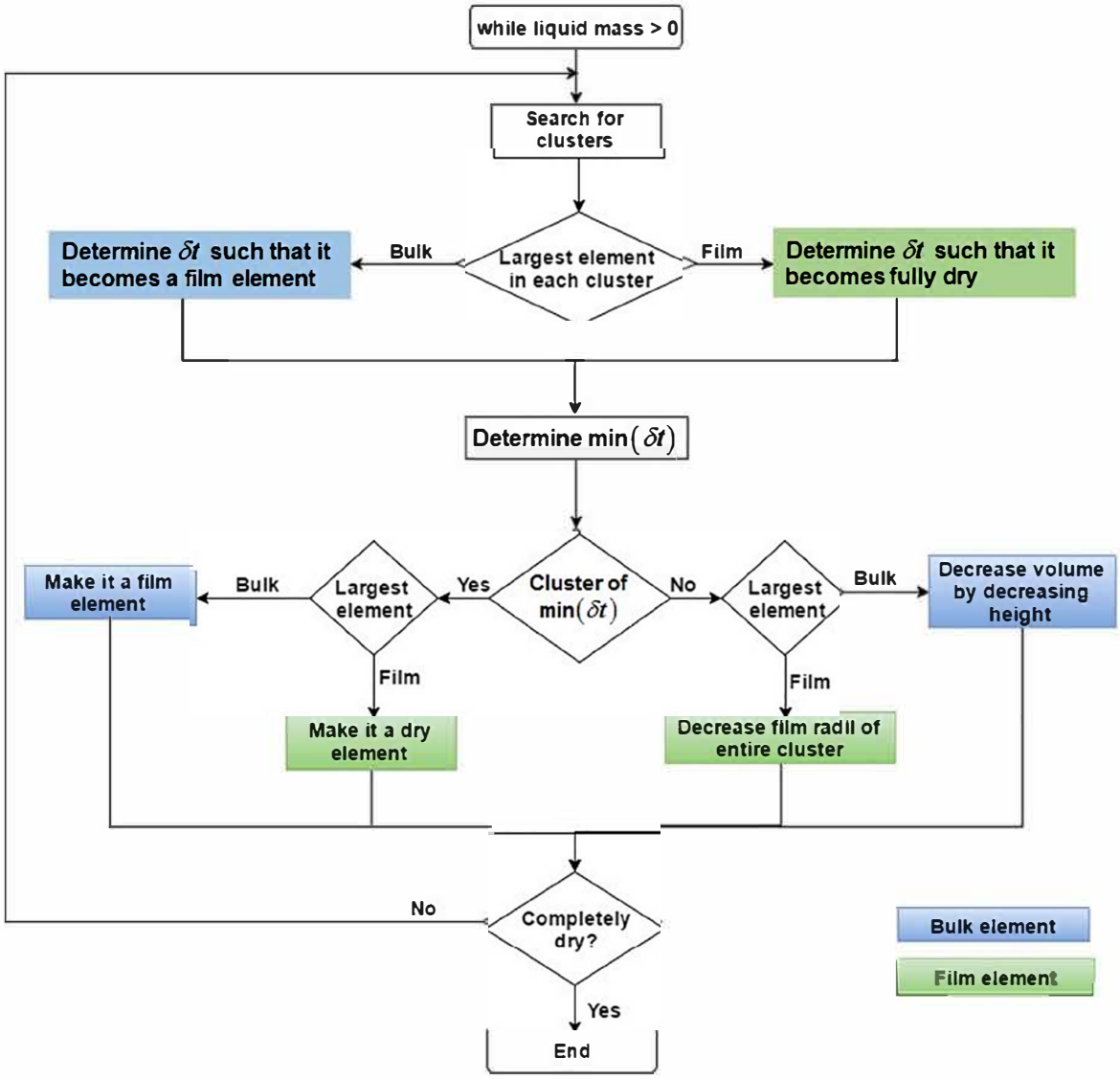

Fig. 3. Flowchart of the cluster-based drying algorithm, where δt is the time step size.

6. Set time step as δt $min(t_{cl}^i)$.
7. In the cluster that has the element which corresponds to $min(t_{cl}^i)$, set to zero the volume of liquid (V_{lt} 0) in the element if it is a film element. Set the volume of liquid in the element to film volume (V_{lt} V_{lf}) if it is a bulk element.
8. In all other clusters, update the liquid content as follows. If it is a cluster with only film elements, decrease the film thickness of all elements in the cluster, according to the mass conservation condition $m_{cl}^i\left(r_{nw,cl}^i(t+\delta t)\right)$ $m_{cl}^i\left(r_{nw,cl}^i(t)\right)$ $F_{cl}^i(\delta t)$. If it is a cluster whose largest element is a bulk element, decrease the liquid volume in that element so as to ensure mass conservation.
9. Determine the new total liquid mass in the network, $m(t+\delta t)$ $\sum m_{cl}^i$.
10. Update time, t $t+\delta t$.
11. Go back to step #1 until $m(t+\delta t)$ 0. The new iteration proceeds with possibly a different cluster configuration and a new mass fraction distribution field.

A few points regarding the proposed drying algorithm are noted. When the gas invasion resulting from evaporation takes place in a bulk element, the capillary pressure varies. This has an impact on the film thickness since the film thickness directly depends on the capillary pressure. Since the size of the bulk element invaded at each invasion step varies, frequent variations of the film thickness are expected with some liquid transfer between the bulk elements and the films. This phenomenon of capillary driven reconfiguration of the films in the clusters is not taken into account. Since the initial film thickness in a throat is dictated by the size of the throat (as stated in step #5) and therefore varies from one film element to the other, the capillary equilibrium over the film subnetwork is not enforced. Nevertheless, it is expected that the liquid mass in the films is reasonably representative with the adopted procedure. While the effect of gravity on the initial film thickness is taken into account using Eqs. (7) and (11), the influence of gravity on the evolution of film thickness during drying is neglected. This is because, as drying progresses, large liquid clusters break up into multiple smaller clusters, thereby negating the effect of gravity within each cluster. Moreover, the question of film thickness does not arise until the later stages of drying as the bulk elements contain most of the liquid in the pore network in the initial stages of drying, as pointed out in Section 5.1. By the time the film elements contain all the liquid in the network, the clusters start to break up, as mentioned above. Nevertheless, the influence of gravity and of capillary driven reconfiguration of the films in the clusters on the film thickness, during the drying process, present interesting avenues of future research.

3. Material characterization and pore network extraction

Pore network simulations in this study are based on PA11 specimens of dimensions $100 \times 100 \times 100\ mm^3$. PA11 is a type of porous asphalt in which the nominal maximum aggregate size is 11 mm. The three PA specimens are named PA11(1), PA11(2) and PA11(3). The PA specimens are imaged in 3D with an X ray microcomputed tomography (X ray μ CT) setup (μDETECT). In this instrument, the X ray radiation is generated by a micro focus X ray tube from Finetec (model FOMR 300.03Y RT) operating at an acceleration voltage of 300 kV and a tube current of 100 μA. A 1 mm thick filtration plate made of copper is placed in front of the source for hardening the beam. The projection images are acquired by a flat panel detector from Perkin Elmer (model XRD 1611 CP3) used in its 2×2 binning mode, corresponding to pixels of 200 μm. An acquisition time of 2.5 s is employed and a total of 4 frames are averaged per orientation of the sample. The sample is rotated in 1600 steps around a fixed axis in steps of 0.225°. The radiographs are corrected for ring artefacts with adequate image processing techniques. A median filter of radius 3 is applied to the images, which are then reconstructed using an in house implementation of the Feldkamp Davis Kress algorithm [44]. The resulting volumes have a voxel size of approximately $72 \times 72 \times 72\ \mu m^3$.

The X ray μ CT images of the specimens are then segmented by thresholding to extract the pore space of PA. The pore networks are extracted from the segmented X ray μ CT images using the modified maximal ball algorithm of Dong & Blunt [45], which is an extension of the work of Silin & Patzek [46]. The maximal ball (MB) algorithm works by fitting the largest possible spheres, centered on each air voxel, such that the spheres just touch the solid boundary. Spheres that are completely inscribed within other spheres are removed and the remaining spheres are called maximal balls, where the largest maximal balls are considered as pores and the smaller balls between them are considered as throats. In Fig. 4, for illustration purposes, pore network extraction from a small region of interest of $12 \times 12 \times 8\ mm^3$ from PA11(1) is shown. In Fig. 5(a) and (b), the pore size distribution (PSD) and throat size distribution (TSD) respectively of the 100 mm cube of PA11(1) is given, as calculated by the MB algorithm. The distributions of the other two specimens are similar and are therefore not shown here. The MB algorithm showed instabilities for datasets larger than $85 \times 85 \times 85\ mm^3$ and, therefore, the pore networks in this study are extracted from a volume of $85 \times 85 \times 85\ mm^3$ from the center of the specimens. Additionally, extracting the pore network from the center of the specimens helps to avoid the edge effect issues that are commonly encountered in pore network extraction. Although the MB algorithm generates an unstructured pore network, structured pore networks (cubic lattices) generated using the Weibull fit parameters estimated from the PSD and TSD histograms are used for the simulations in this study.

Weibull probability distribution functions are often used to model the pore space characteristics of porous media [47,48]. The histograms in Fig. 5(a) and (b) are fitted with a two parameter Weibull probability distribution function (PDF), which is given by the red curve in the figures. The two parameter Weibull PDF is defined as:

$$f(d_0;\alpha,\beta) \quad \begin{cases} \beta\left(\frac{d_0{}^{\beta}\ 1}{\alpha^{\beta}}\right) exp\left(\quad \left(\frac{d_0}{\alpha}\right)^{\beta}\right), & d_0 \geq 0 \\ 0, & d_0 < 0 \end{cases} \tag{12}$$

In Eq. (12), d_0 is the pore diameter while α and β are the scale and shape parameters, respectively, of the Weibull distribution. The scale parameter defines the width of the distribution while the shape parameter, as the name implies, defines the shape of the distribution. For PA11(1), PA11(2) and PA11(3), the Weibull parameters for PSD are α $1.149, 1.064, 1.120$ and β $1.264, 1.254, 1.076$. The corresponding parameters for TSD are α $0.721, 0.606, 0.791$ and β $1.313, 1.370, 1.280$. The next step is to quantitatively assess whether the distributions are adequately captured by the Weibull distribution. This is done by means of a probability plot, in which the cumulative distribution function (CDF) of the distribution, whose scale and shape parameters are determined from the histogram fits, is plotted against the data points in a log log plot. If the data points are predicted well by the distribution, then these points should overlap with the straight line in the probability plot, as shown in Fig. 5(c) and (d). The ordinate of the probability plots is a rearranged form of the Weibull CDF, defined by the following equation:

$$log\left[ln\left(\frac{1}{1 \quad F(d_0)}\right)\right] \quad \beta log(d_0) \quad \beta log(\alpha). \tag{13}$$

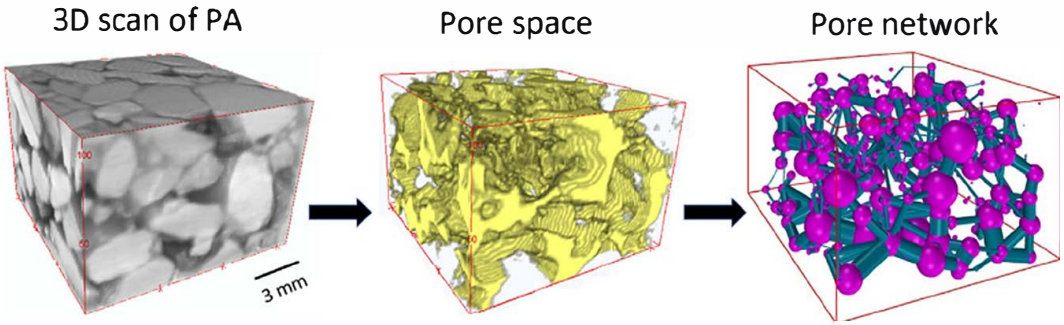

Fig. 4. Work flow of the pore network extraction process. First, the 3D X-ray μ-CT scan is segmented to obtain the pore space, followed by pore network extraction of the pore space using the Maximal Ball algorithm [45]. A region of interest of 12 × 12 × 8 mm³ of the specimen PA11(1) is used for this illustration.

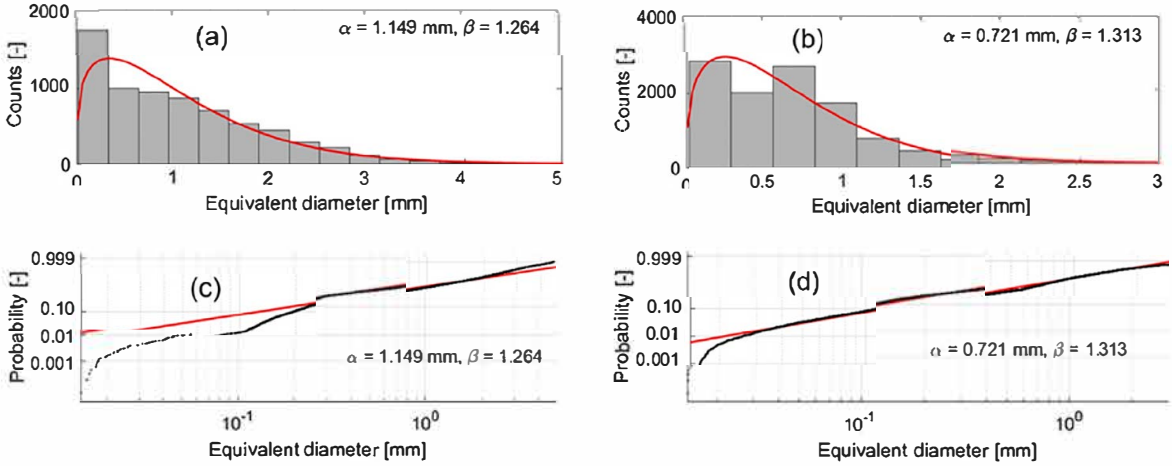

Fig. 5. Histograms of (a) pore size distribution (PSD) and (b) throat size distribution (TSD) of PA11(1) fitted with a two-parameter Weibull distribution (red curve); and cumulative probability plots of (c) PSD and (d) TSD histograms where the red line indicates the predicted distribution while the points represent the data underlying the histogram. The scale (α) and shape (β) parameters of the fit are given in the respective graph.

If $y \quad ln\left(\frac{1}{1-F(d_0)}\right)$, then $log(y)$ is linear to $log(d_0)$ with slope β and intercept $\beta log(\alpha)$. This linear relationship is indicated by the red line in Fig. 5(c) and (d), along with the original data (points) from the histograms in Fig. 5(a) and (b).

The values of α and β give physical insights into the pore and throat sizes of PA. In a two parameter Weibull distribution, α can be interpreted as the value below which 63.2% of all observations fall, irrespective of the value of β. The values of α for PSD (≈1.1 mm) and TSD (≈0.7 mm) are similar between the three specimens. A significant number of pores with 2 4 mm diameters and throats with 1 3 mm diameters are seen in the specimens. These large pores and throats are primarily responsible for the excellent drainage properties of PA. From Fig. 5(c) and (d), it is seen that Weibull distributions accurately represent the PSD and TSD of PA11(1) as most of the data points fall on the straight line of the probability plots. It should be noted that in a probability plot, data points at low probability values will never fall on a straight line since the number of data points is finite.

Using the PSD and TSD distribution parameters of the specimens, cubic lattice pore networks are generated. A constant connectivity of 6 is assumed for all throats as it is the simplest connectivity for a cubic lattice. A constant lattice length of 5 mm is given to make the overall pore network dimensions equal to the specimen size of 85 × 85 × 85 mm³ while the pore lengths are assumed to be equal to the respective inscribed circle diameters. The average void space of the three pore networks is 48 × 10 ^{6} m³. Considering that the specimen size of the PA that was used to generate the pore network is 85 × 85 × 85 mm³, it implies that the pore (void) network has a volume fraction of 8%. Normally, PA slabs have a void fraction of 15 20%. However, since the specimens for generating the pore network are cut from the center of large slabs, their void fraction is expected to be lower than 15 20% as most of the void space is at the slab edges. Additionally, the 'effective' void fraction in the real material is expected to be lower than 15 20% since some pores are inaccessible to water, while all the elements in the pore network can be potentially invaded by water. Therefore, a pore network with 8% volume fraction can be considered realistic to represent the macroscopic dying behavior of PA.

Equilateral triangular pores and throats are used in the pore network i.e. the corner half angle, $\alpha_c = 30°$, and number of sides, N_c 3. A triangular cross section is used since arc menisci can exist in an angular geometry only if the criterion $\theta < \frac{\pi}{N_c}$ is met [33], where θ [°] is the solid liquid contact angle. Note that the specimens are cut from a freshly compacted slab of PA. In a fresh PA specimen, where most of the aggregates are covered by bitumen, the representative contact angle should ideally be 99 106° as this is the water bitumen contact angle range [49]. Such a high contact angle is not compatible with the existence of trapped liquid in corners. Thus, it is assumed the liquid films formed in regions without bitumen where the liquid is in direct contact with the aggregates used in PA. Therefore, $\theta = 55°$ is assumed for the simulations in this study as this is the approximate contact angle between water and the aggregates used in PA [50]. Given $\theta = 55°$,

only a triangular geometry satisfies the condition for corner flow. Moreover, the use of pore shapes such as squares and hexagons will result in further reduction of the pore network void space as compared to the void space in the real specimen, given similar net work complexity. For simplicity, equilateral triangles are used which implies that the shape factor G 0.048.

4. Drying experiments

Drying in conventional microporous media usually exhibits a first phase of rapid drying, called transition period (TP) [51], fol lowed by the constant drying rate period (CDRP), during which liq uid continuity is ensured through corner films, even if the percolation front i.e. the bulk air infiltration front, does not have a macroscopic connectivity from the surface to the bottom. These liquid films ensure a constant supply of liquid to the surface during CDRP and therefore the drying rate remains constant during this period as, at the surface, the moisture content lost by evaporation is replaced by liquid flow arriving from within the material. During CDRP, the drying rate is therefore determined by the boundary layer thickness of the convecting fluid. Once the surface starts to become dry, the hydraulic connectivity from corner films starts to break down as the tips of the films recede deeper into the mate rial. The drying rate at this stage starts to progressively decrease and is therefore called decreasing drying rate period (DDRP). Dur ing DDRP, the drying rate is determined by the effective diffusivity of water vapor within the material.

To gain first insights about drying in a macroporous media such as PA, gravimetric experiments of drying of PA11(1), PA11(2) and PA11(3) are carried out. The same specimens of dimensions $100 \times 100 \times 100$ mm^3 from which the pore networks for the PNM simulations are extracted are also used for the experiments. The specimens are first submerged in water for at least 24 h. There after, they are taken out and water is allowed to drain from all sides for 2 h. Then the specimens are placed in a polystyrene foam box that is closed on all sides except the top, similar boundary con ditions will be used in the PNM simulations presented in the next section. The moisture loss from the specimens is then monitored until they are completely dry. The drying experiments are carried out in a controlled environment of 23 °C and 65% relative humidity. Precursor laboratory experiments performed on similar specimens under the same experimental conditions showed that temperature gradients within PA during the drying process is negligible (<0.2 °C). Temperature was measured at the lateral edges and at the center of a PA11 specimen with eleven thermocouples, two each at the four lateral edges and three at the center. Therefore, the assumption of isothermal drying in the PNM simulations is found to be valid, at least for the experimental conditions in this study.

In Fig. 6, the results of the drying experiments of the three PA specimens are presented in terms of the temporal evolutions of normalized moisture loss and of drying rate. Here, the normalized moisture loss is calculated as m_{loss} $\frac{(m(t_0)\ m(t))}{m(t_0)}$ i.e. moisture loss normalized by the initial moisture mass of the specimens. The dry ing rate is defined as $\dot{m}_{dry}$ $(m(t_0)\ m(t))/t$. The TP and DDRP of PA11(1) are indicated in Fig. 6(b). During TP, a sharp drop in the drying rate can be seen as water in the top pores dries very quickly, first in the large pores and then in the smaller pores. At the end of TP, only a few liquid paths exist in the material that are connected to the environment. Unlike drying in conventional porous media, the drying process in PA completely skips CDRP and goes from TP to DDRP, as marked in Fig. 6(b). This is because of two reasons: first, due to the strong influence of gravity, most of the residual water after drainage is concentrated at the lower regions of PA specimens as the static pressure head is low at lower heights and, second, the capillary transport of water within the material is not sufficient to feed the evaporating surface so as to balance the rate of evaporation from the surface. This is yet another indica tion that fluid transport in PA cannot be modelled akin to that in conventional microporous media, where the presence of CDRP dur ing the initial stages is quite common even in materials where gravity effects are significant [2]. In some cases [2], after the DDRP, a second CDRP may be observed in conventional porous media when the liquid flow in film regions is primarily driven by gravity instead of capillary pressure gradients. In such cases, the evapora tion front is observed to remain stationary leading to a constant evaporation rate. This phenomenon is also not seen in PA.

5. PNM simulations of drying and sensitivity analysis

In this section, the results of the pore network model (PNM) simulations of drying of the three PA11 specimens described in the previous sections are presented. At the start of the experi ments, pores can have different states and should be assigned an initial status. This is done via hydrophobic, hydrophilic and dead end elements, the relative proportions of which are seen later to be an important parameter that acts as a control variable in the simulations. As stated earlier, the contact angle cannot be given a value larger than 60°, which implies that all pores are hydrophilic by default. Unsaturated wet hydrophilic pores are represented as

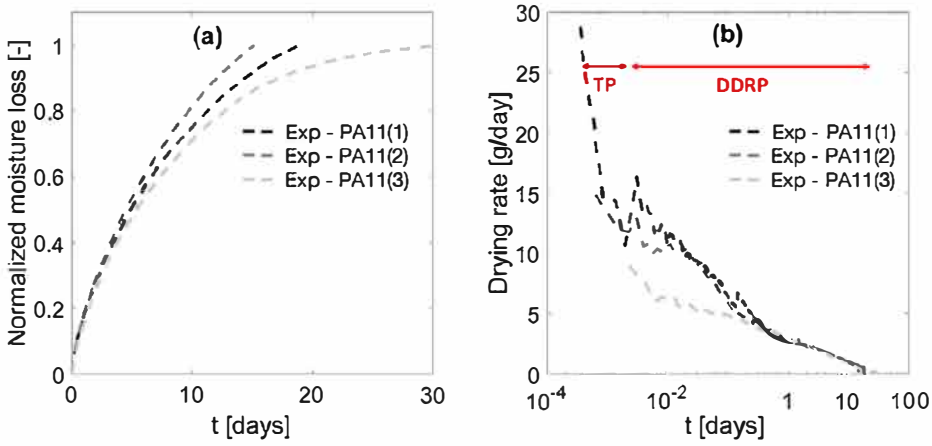

Fig. 6. Experimental results of drying presented in terms of (a) normalized moisture loss and (b) drying rate as a function of time (note the log scale for time), for specimens PA11(1), PA11(2) and PA11(3). The transition period (TP) and decreasing drying rate period (DDRP) of PA11(1) are indicated in (b).

film elements. Hydrophobic pores that are already dry and dead end elements that are liquid saturated at the beginning of drying are indirectly taken into account in the network by specifying a certain number of elements as dry and bulk elements respectively. Ultimately, the proportions of dry, bulk and film elements in the network determine the residual liquid content and its distribution in the network at the beginning of drying. Since the real proportion of these element types in PA is unknown, for the drying simulations in this study, the proportions are chosen in such a way that the residual liquid contents in the pore networks after drainage match those measured during the gravimetric experiments presented earlier.

5.1. Drying in PA pore networks

The evaporation of water in PA pore networks is modeled with the drying algorithm described in Section 2.2, under the same conditions of the gravimetric experiments. Similar to the experiments, all the lateral surfaces as well as the bottom surface of the network are assumed to be impervious. Vapor transfer occurs only at the top surface of the network, where the effect of the air boundary layer is applied using Eq. (10) i.e. the transfer of vapor from the top surface to the environment is assumed to take place through a diffusive layer of uniform thickness δ. At temperatures close to 20 °C, $\delta \approx 10^{-4}$ 10^{-3} m for a vapor air system [33]. In the simulations in this study, $\delta \approx 10^{-3}$ m is assumed, the implications of which are later discussed in detail. The environmental vapor mass fraction is taken as c_∞ 0.011, which is the vapor mass fraction at a temperature of 23 °C and relative humidity of 65%, the saturation vapor mass fraction c_e 0.018 at 23 °C, and the film thickness cut off factor η 0.01. The value for η is chosen somewhat arbitrarily based on the criterion that elements are considered dry when their film thickness is small enough to not influence the drying process any further. The other fluid properties used are: γ 0.027 N/m, ρ_g 1.184 kg/m³ and ρ_l 1000 kg/m³, which are standard water and air properties at 23 °C.

A two dimensional schematic of the expected distribution of water in the pore network at the beginning of drying is given in Fig. 7. At this stage, all pores and throats that are directly connected to the six boundary faces of the cubic lattice are assumed to be completely dry. This assumption is justified as all sides of the PA11 cubic specimens are also open, during draiange, in the validation experiments presented in the previous section. Due to a high static pressure head, the elements near the top surface are especially conducive to air entry. Moreover, this step also introduces a certain degree of hydrophobicity into the network by not retaining any water in certain pores. As stated before, since PA is a mostly hydrophobic material, most of the residual liquid content after drainage is expected to be in the dead end pores or trapped in hydrophilic pores. Therefore, a majority of the elements, i.e. around 60 70% of the total number of elements, depending on the specimen, are specified to be fully saturated at the beginning of drying. The remaining elements either retain water in their corners or are completely dry if they are directly in contact with the boundaries. This allowed the liquid content in the pore networks at the beginning of drying to be approximately equal to the observed liquid mass at the beginning of drying in the validation experiments. Due to the slight but present difference in pore space volumes of the specimens and the generated pore networks as mentioned earlier, the drying rates in this study are analyzed as a function of time, and not as a function of saturation.

In Fig. 8, the results of the PNM simulations of drying of the three specimens are presented in terms of the temporal evolutions of normalized moisture loss and drying rate, similar to Fig. 6. The overall drying times of the three specimens in the simulations are 18, 18 and 22 days, while their corresponding time in the experiments (Fig. 6) are 19, 15 and 30 days. Although PA11(3) dries faster in the simulations, it is seen that by the 22nd day in the experiments, only less than 5% of the initial moisture content is left in PA11(3). So the overall agreement between the experiments and simulations in terms of the total drying time is fair. In Fig. 8(b), two drying rate periods can be clearly distinguished in the PNM simulations and they are marked in the figure. For specimens PA11(1) and PA11(2), until $t = 7$ days, the drying rate is constant i.e. the drying regime is CDRP. For PA11(3), CDRP is seen until $t = 10$ days. After that period, the drying rate constantly decreases until the material is almost dry i.e. the drying regime is DDRP. The lower drying rate of PA11(3) during CDRP is also seen in Fig. 8(b). The comparison of the PNM and experimental results is done later in

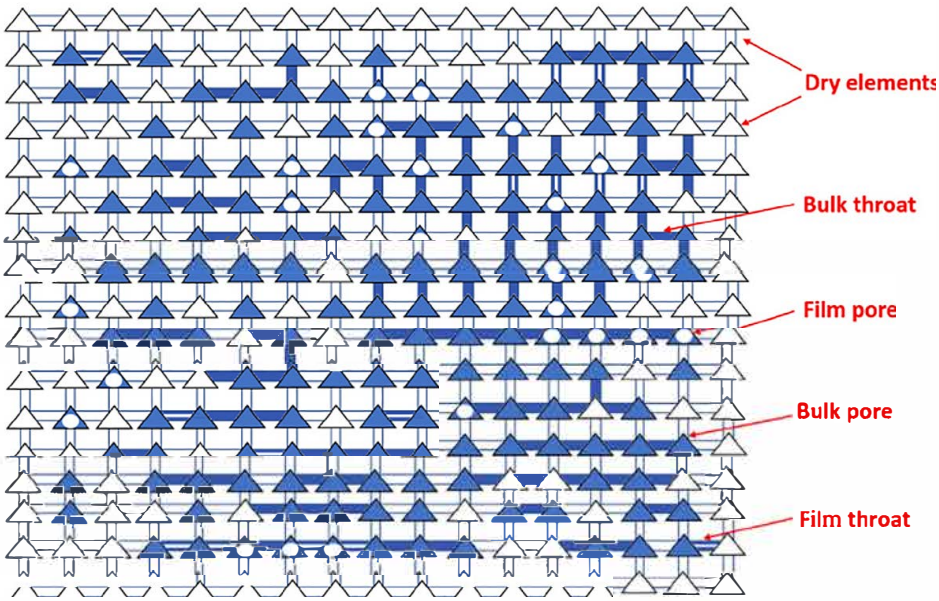

Fig. 7. 2D schematic of the initial water distribution in the pore network at the beginning of drying. Features of the network such as dry boundaries, bulk/film pores and bulk/film throats are indicated.

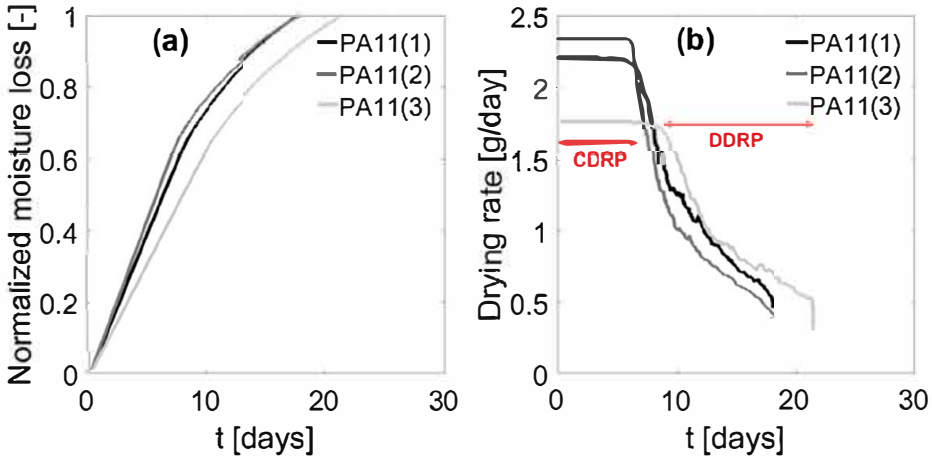

Fig. 8. (a) Pore network modeling (PNM) results of normalized moisture loss and (b) drying rate as a function of time for specimens PA11(1), PA11(2) and PA11(3). The constant drying rate period (CDRP) and the decreasing drying rate period (DDRP) of one of the specimens, PA11(3), are indicated in (b).

Section 5.4. The critical water saturation at which the drying regimes transition from CDRP to DDRP in PA11(1), PA11(2) and PA11(3) are 0.26, 0.22 and 0.15 respectively.

5.2. Homogeneity of moisture content distribution during drying

The drying algorithm developed in this study is not expected to result in a top down drying gradient in the network as the algorithm is based on a cluster based invasion process. In other words, the proximity of a wet element to the open surface is not the only factor influencing its drying rate. To check if any drying gradients develop during the simulations, additional simulations are performed on a smaller domain, a $12 \times 12 \times 12$ network with pore diameters, throat diameters and throat lengths similar to those of the PA11(1) network. This network achieves a balance between computational speed and mimicking the same drying pattern as seen in the larger $17 \times 17 \times 17$ network. It is to be noted that the absolute values of the results from the simulations using the $12 \times 12 \times 12$ network is not representative of PA, and the simulations using this network serve to obtain only a qualitative picture of the drying process and the trends therein, which is similar to that in PA.

In Fig. 9, the liquid saturation S_w in the network is monitored throughout the drying process by dividing the network into a 12×12 checkerboard grid, with each grid representing all 12 pores in the out of plane (depth) direction. To enable a comparison between this smaller grid and the larger grid of the real PA simulations, time steps are normalized with the total drying time, t_{tot}. In Fig. 9, no significant drying gradient can be seen in the network at any stage of the drying process. The absence of a drying front in PA is also observed in previous neutron radiography experiments [5]. At the beginning of drying, there is just one large liquid cluster spanning the entire volume of the network. According to the algorithm, the elements near the open surface have to dry first since there is only one cluster and these are the elements that happen to be at the edge of the cluster. However, as drying progresses, the number of liquid clusters in the network also starts to increase. In such a scenario, the proximity of an element to the open surface starts to matter less, the drying ceases to be top down, and as a result there is no identifiable pattern of drying.

Revisiting Fig. 8(b), the occurrence of CDRP until $t = 7$ days for PA11(1) and PA11(2) and $t = 10$ days for PA11(3), and DDRP thereafter, cannot be attributed to the drying physics in conventional microporous media. Rather, the observed drying behavior can be attributed to the assumption of a connected film path in the drying model. An underlying principle of the drying algorithm is the two step drying process i.e. in a cluster with both bulk and film elements, bulk elements lose moisture first and become film elements. Therefore, during CDRP, most of the moisture loss occurs as a result of bulk elements becoming film elements. An important assumption in the drying algorithm is that the mass fraction in a pore adjacent to a throat containing liquid is the saturation vapor mass fraction, c_e. Due to this assumption, during CDRP, $c \quad c_e$ in most of the pores as they are adjacent to wet throats. As a result, evaporation is confined to the top region of the network as only the pores and throats near the surface are capable of transporting vapor to the environment. At this stage, vapor diffusion within the network is totally controlled by the diffusion happening across the external transfer length, δ. As a result, the drying rate remains constant as δ is assumed to be constant throughout the simulations.

After CDRP, the film elements begin to dry, vapor has to travel longer distances within the network before exiting the porous medium, and therefore the drying rate starts to decrease. This explanation is further discussed in the next section. The observed drying rate in the simulations also implies that the drying at the beginning is sensitive to the value of δ. An exact quantification of δ for a very rough and permeable surface like that of PA is a challenging task and is another promising avenue for future studies.

5.3. Sensitivity analysis of the presence of corner films

The influence of considering corner films on the drying rate in the developed model is investigated in Fig. 10 by analyzing the temporal evolutions of normalized moisture loss and drying rate for two cases, with and without corner films in the network. The smaller $12 \times 12 \times 12$ network presented in the previous section is used in this study as well. The simulation with corner films has 40% (saturated) bulk elements and 60% film elements at the beginning of drying while the simulation without corner films has 40% (saturated) bulk elements and 60% dry elements at the beginning of drying. The initial moisture content at the beginning of drying is only slightly higher for the former case. In the absence of films in the network, the drying algorithm is slightly modified. The initial steps of the algorithm are essentially the same i.e. identifying clusters, determining the vapor flux from each cluster, identifying the largest element in each cluster and then choosing the element among them that will dry the fastest. The difference is in the fact that this chosen element is completely dried in the given time step (instead of becoming a film element), and the largest elements in all other clusters dry partially such that mass conservation is ensured. The influence of such an approach on the drying rate is strikingly visible in Fig. 10. While the network with film

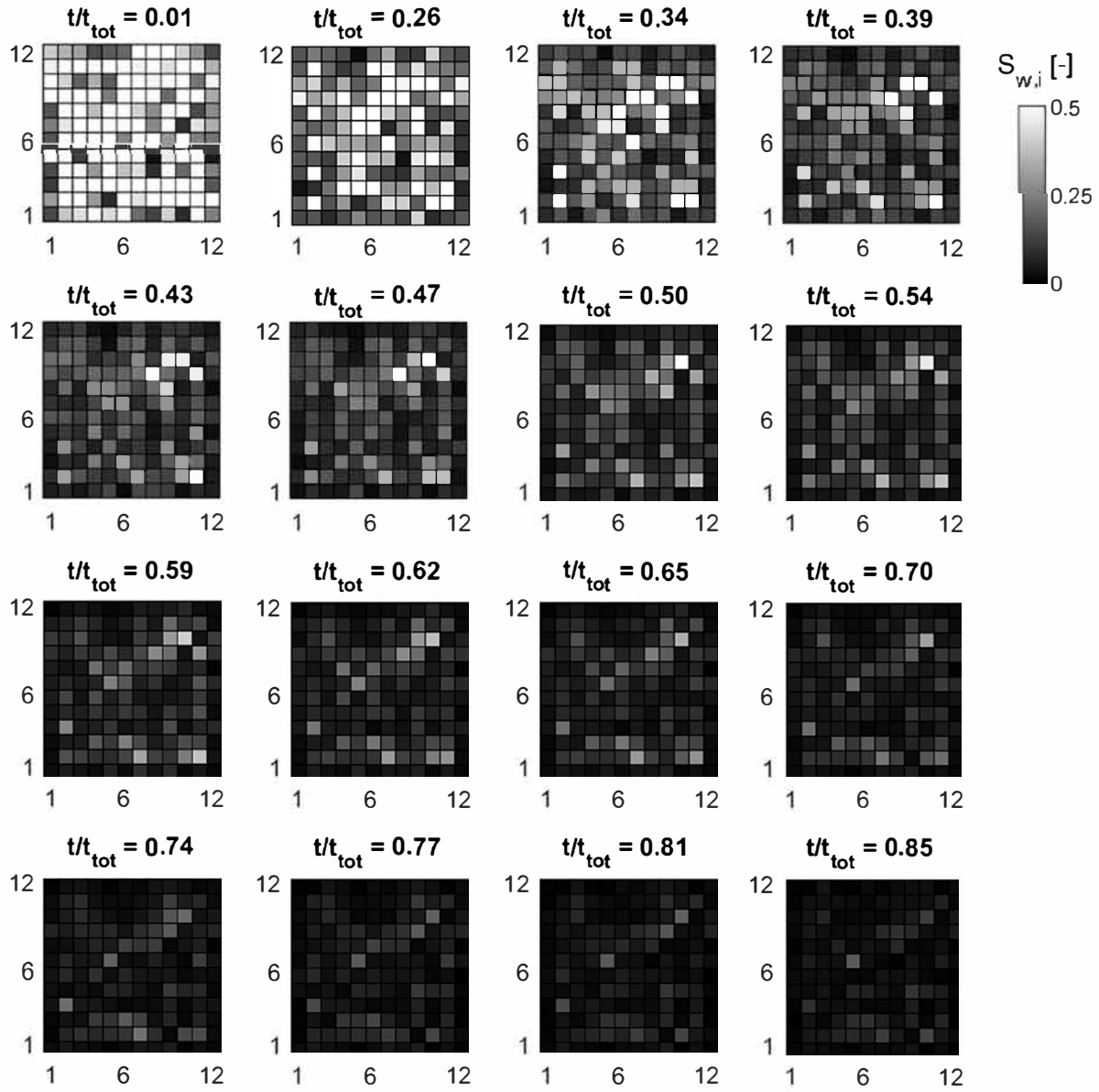

Fig. 9. Checkerboard pattern of drying in the pore network with time steps indicated above each figure. The domain is divided into 144 equisized grids and the grid color indicates the water saturation $S_{w,i}$ at the grid along the entire thickness (out of plane direction) of the network.

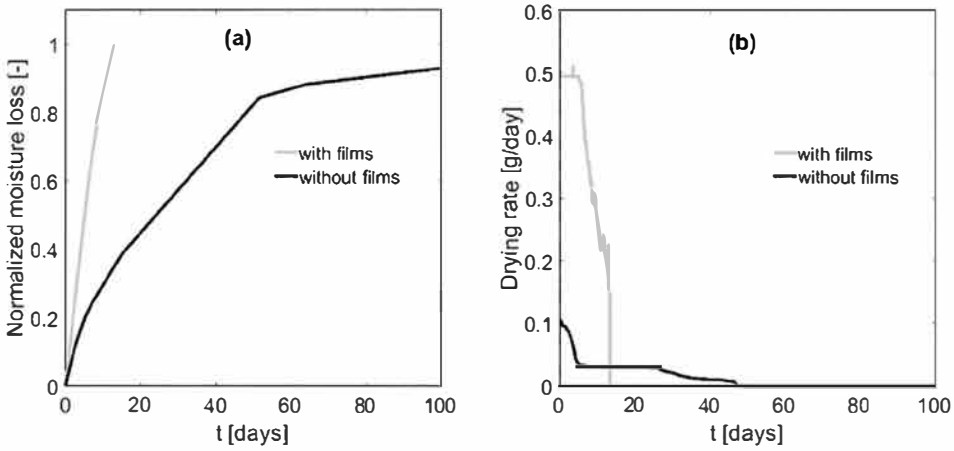

Fig. 10. Effect of corner films on drying as seen from the temporal evolutions of (a) normalized moisture loss and (b) drying rate.

flow completely dries out in 13 days, the network without film flows starts drying at a lower rate and at $t = 48$ days, the drying rate in the absence of films becomes extremely small. In Fig. 10 (b), it can be seen that drying without films begins with DDRP, similar to what is observed in the experiments presented in Section 4, but at a much lower rate. This proves that the CDRP at the beginning of the simulations with film flow is due to the over prediction of film elements in the PA pore network. However, simulating drying without considering any film elements will lead to a large under prediction of the drying rate.

5.4. Comparison of PNM simulations with experiments

The results from the experiments (Fig. 6) and PNM simulations (Fig. 8) of drying are compared in Fig. 11. In Fig. 11(a), a fair agreement can be seen between the simulations and the experiments for the drying of PA11(1) and PA11(2). For PA11(3), the agreement is not as good because the resistance of PA11(3) to drying is the highest, as seen in the experiments. In Fig. 11(b), the drying rates of the experiments and simulations are compared after excluding the transition period (TP) of the experiments, marked in Fig. 6(b), for better visualization. While the drying rates of the experiments and simulations are largely similar after $t = 7$ days for PA11(1) and PA11(2), those of PA11(3) show a difference, as expected. The large difference in the drying rates of the experiments and simulations in the first 24 h of drying can be attributed to the difference in the initial liquid configuration at the beginning of drying. While the hydraulic connectivity within the specimens seem to be very low at the beginning of the experiments, leading to the onset of DDRP, the initial drying in the simulations is concentrated at the top region of the specimen. This leads to CDRP in the simulations as observed in Fig. 8(b). However, as pointed out earlier, the latter half of the drying process in the PNM simulations from $t = 7$ days onwards shows good agreement with the experiments as, by this time, the long vapor diffusion path in the real PA pore structure is also reflected in the simulations.

Previous experiments of drying in PA [4,5] have pointed to the limited impact of liquid redistribution on drying in PA. However, the initial pattern of liquid distribution in PA at the beginning of drying has a definite influence on the drying algorithm presented in this paper. As drying progresses, drying becomes increasingly dictated by vapor transport and less by the exact liquid configuration. This could be an important reason why there is a good agreement of the experiments and simulations during the second half of the drying process. In other words, the second half of the drying process is strongly driven by vapor partial pressure gradients. At this stage of drying, the structural properties of the material such as porosity and tortuosity are more important than the connectivity of the liquid clusters. The good agreement between the experiments and simulations at this stage points to the efficiency of the simplified pore network extracted from the CT scans of the specimens. The use of an unstructured pore network may therefore result in an even better representation of the drying kinetics in PA and presents an interesting avenue of future research.

Since PA is a complex composite material with a range of wettability and pore sizes, modeling drying in PA using PNM is not a trivial task. Though a few simplifications and assumptions are made in the drying model presented in this study, we believe that a significant first attempt has been made to model drying in a macroporous material in which the drying physics seen in conventional porous media, in particular distinct drying regimes, are not fully applicable. The cluster based drying algorithm developed in this study captures part of the drying behavior of PA and is a promising first step towards developing robust pore network models of drying in highly complex, macroporous media. The model also stands to gain with a more realistic pore network extraction which, in particular, captures accurately the connectivity of the large pores in PA, since large pores that are highly connected will have a significant impact on the drainage and drying processes in macroporous materials.

6. Conclusions

A pore network model (PNM) of drying in a gravity dominated macroporous medium, porous asphalt (PA), is developed. The pore and throat size distributions of the networks in the simulations are obtained from X ray μ CT scans of PA. Drying of liquid from PA is simulated with PNM using a cluster based approach with a two step drying process i.e. elements transform from being fully saturated, to having liquid only in the corners of the pores and the throats, to finally becoming completely dry. This approach is markedly different from previous modelling of liquid films in drying PNM [30 33] and is based on a completely different view as regards the role of the films in terms of hydraulic interconnectivity between liquid clusters. However, the overall results (see point # 2 below) is not sufficient to really indicate which of the two options, i.e. strong effect on the hydraulic connectivity between clusters as in our model or no hydraulic connectivity at all via the films as in the previous models, is more relevant. Additionally, it is also diffi

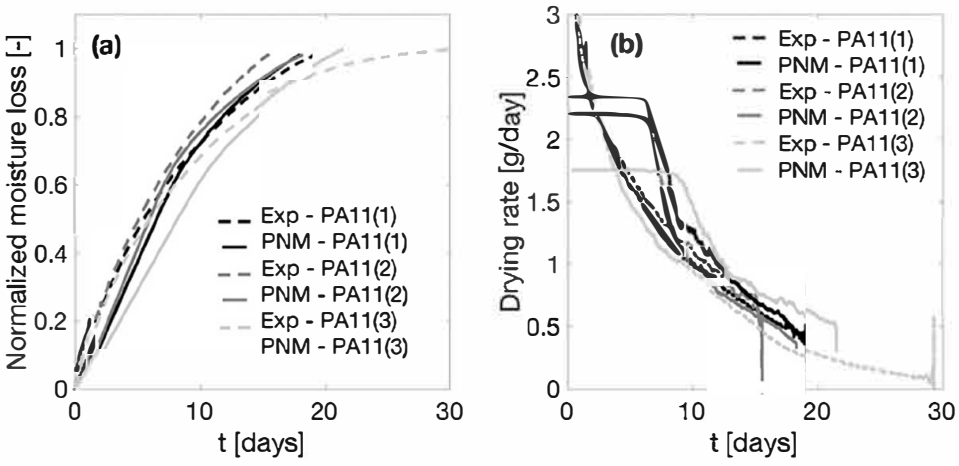

Fig. 11. Comparison of experimental and pore network modeling (PNM) simulations of drying presented in terms of (a) normalized moisture loss as a function of time, and (b) first derivative of the moisture loss (drying rate) as a function of time, with the time period of the experimental data starting from $t = 1.5$ days for better visualization, for specimens PA11(1), PA11(2) and PA11(3).

cult to readily conclude from the experiment whether the liquid trapped in the corners really forms a secondary flow system extending over a long distance or not. As discussed in Vorhauer et al. [52], disconnected film systems, i.e. rings, can also form depending on the pore geometry and contact angle. For instance, the fact that there is no significant constant drying rate period in the experiments might be an indication that the films form disconnected clusters rather than an interconnected system spanning over a large region.

In addition to the modeling question, the most important conclusions from this study are:

1. From experiments, it is seen that drying in a strongly macroporous material such as PA completely skips the first drying phase, the constant drying rate period (CDRP), and instead begins with the second drying phase, the decreasing drying rate period (DDRP). This can be explained as a consequence of the large pores drying out fast and a low hydraulic connectivity of the other pores in PA. The drying rate in the experiments show a steep drop within the first 24 h of drying.
2. The drying experiments and PNM simulations show a fair overall agreement for two of the three specimens investigated. The third specimen has a very high resistance to drying and this is not captured by the PNM model. The PNM simulations exhibits CDRP initially and transitions to DDRP thereafter. In the second half of the drying period, the drying rates of experiments and simulations show good agreement for the two specimens with lower drying resistance. A detailed analysis showed that the CDRP at the beginning of the PNM simulations is due to the assumption of film flow in the network, and its duration can be minimized by increasing the initial number of dry elements in the network, when representing the water distribution after drainage. Although interesting, this comparison is, however, not sufficiently accurate for really assessing the relevance of the proposed PNM with corner films. In particular, several assumptions (no gravity or viscous effects taken into account in the film model, no consideration of the capillary driven reconfiguration of the liquid in the films after each invasion, impact of the films on the hydraulic conductivity between clusters) need specific evaluations either through comparison with direct numerical simulations or microfluidic experiments. Clearly, more work is needed to take into account liquid film effects in PNM.
3. The need to represent the pore space of PA more accurately using pore networks is identified in the results. Specifically, a more accurate knowledge of parameters such as wettability distribution of the solid matrix of PA, pore connectivity, especially of large pores, and liquid distribution at the onset of the drying, will help to make the drying model developed in this study more representative of the drying behavior in real macroporous materials.

Declaration of Competing Interest

The authors declared that there is no conflict of interest.

Acknowledgment

This research was supported by a Swiss National Science Foundation (SNF) Grant (200021_143651).

References

[1] A.G. Yiotis, I.N. Tsimpanogiannis, A.K. Stubos, Y.C. Yortsos, Pore-network study of the characteristic periods in the drying of porous materials, J. Colloid Interface Sci. 297 (2) (2006) 738–748.
[2] A.G. Yiotis, D. Salin, Y.C. Yortsos, Pore network modeling of drying processes in macroporous materials : effects of gravity, mass boundary layer and pore microstructure, Transp. Porous Media 110 (1) (2015) 1–22.
[3] S. Lal et al., Investigation of water uptake in porous asphalt concrete using neutron radiography, Transp. Porous Media 105 (2) (2014) pp.
[4] S. Lal et al., Investigation of gravity-driven drainage and forced convective drying in a macroporous medium using neutron radiography, Transp. Porous Media 118 (1) (2017) 119–142.
[5] S. Lal et al., Wetting and drying in hydrophobic, macroporous asphalt structures, Constr. Build. Mater. 152 (2017).
[6] S. Lal, P. Moonen, L.D. Poulikakos, M.N. Partl, D. Derome, J. Carmeliet, Turbulent airflow above a full-scale macroporous material: boundary layer characterization and conditional statistical analysis, Exp. Therm. Fluid Sci. 74 (2016) 390–403.
[7] S. Lal et al., CFD modeling of convective scalar transport in a macroporous material for drying applications, Int. J. Therm. Sci. 123 (2018) 86–98.
[8] I. Fatt, The network model of porous media I. Capillary pressure characteristics, Pet. Trans. AIME 207 (Jan. 1956) 144–181.
[9] M. Blunt, M. King, H. Scher, Simulation and theory of two-phase flow in porous media, Phys. Rev. A 46 (12) (1992) 7680–7699.
[10] R. Lenormand, Numerical models and experiments on immiscible displacements in porous media, J. Fluid Mech. 189 (1988) 165–187.
[11] A. Sahni, J. Burger, M. Blunt, Measurement of three phase relative permeability during gravity drainage using CT, in: SPE/DOE Improved Oil Recovery Symposium, 1998.
[12] V. Joekar Niasar, S.M. Hassanizadeh, L.J. Pyrak-Nolte, C. Berentsen, Simulating drainage and imbibition experiments in a high-porosity micromodel using an unstructured pore network model, Water Resour. Res. 45 (2) (2009).
[13] R.G. Hughes, M.J. Blunt, Pore scale modeling of rate effects in imbibition, Transp. Porous Media 40 (2000) 295–322.
[14] T.W. Patzek, Verification of a complete pore network simulator of drainage and imbibition, SPE J. 6 (02) (2001) 144–156.
[15] J.B. Laurindo, M. Prat, Numerical and experimental network study of evaporation in capillary porous media. Drying rates, Chem. Eng. Sci. 53 (12) (1998) 2257–2269.
[16] M. Prat, Recent advances in pore-scale models for drying of porous media, Chem. Eng. J. 86 (5502) (2002) 153–164.
[17] M. Börnhorst et al., Influence of pore structure and impregnation–drying conditions on the solid distribution in porous support materials, Dry. Technol. 34 (16) (2016) 1964–1978.
[18] T. Metzger, E. Tsotsas, M. Prat, Pore-network models: a powerful tool to study drying at the pore level and understand the influence of structure on drying kinetics, in: Modern Drying Technology, Weinheim, Germany, Wiley-VCH Verlag GmbH & Co. KGaA, 2014, pp. 57–102.
[19] A. Rahimi, T. Metzger, A. Kharaghani, E. Tsotsas, Interaction of droplets with porous structures: pore network simulation of wetting and drying, Dry. Technol. 34 (9) (2016) 1129–1140.
[20] V.K. Surasani, T. Metzger, E. Tsotsas, Drying simulations of various 3D pore structures by a nonisothermal pore network model, Dry. Technol. 28 (5) (2010) 615–623.
[21] M. Prat, Percolation model of drying under isothermal conditions in porous media, Int. J. Multiph. Flow 19 (4) (1993) 691–704.
[22] T. Shaw, Drying as an immiscible displacement process with fluid counterflow, Phys. Rev. Lett. (1987).
[23] M. Prat, F. Bouleux, Drying of capillary porous media with a stabilized front in two dimensions, Phys. Rev. E 60 (5) (1999).
[24] I. Tsimpanogiannis, Y. Yortsos, Scaling theory of drying in porous media, Phys. Rev. E (1999).
[25] M. Prat, Isothermal drying on non-hygroscopic capillary-porous materials as an invasion percolation process, Int. J. Multiph. Flow 21 (5) (1995) 875–892.
[26] H.P. Huinink, L. Pel, M.A.J. Michels, M. Prat, Drying processes in the presence of temperature gradients–pore-scale modelling, Eur. Phys. J. E 9 (2002) 487–498.
[27] A.G. Yiotis, A.K. Stubos, A.G. Boudouvis, Y.C. Yortsos, A 2-D pore-network model of the drying of single-component liquids in porous media, Adv. Water Resour. 24 (3–4) (2001) 439–460.
[28] A.G. Yiotis, I.N. Tsimpanogiannis, A.K. Stubos, Y.C. Yortsos, Coupling between external and internal mass transfer during drying of a porous medium, Water Resour. Res. 43 (6) (2007).
[29] N. Vorhauer, Q.T. Tran, T. Metzger, E. Tsotsas, M. Prat, Experimental investigation of drying in a model porous medium: influence of thermal gradients, Dry. Technol. 31 (8) (2013) 920–929.
[30] A.G. Yiotis, A.G. Boudouvis, A.K. Stubos, I.N. Tsimpanogiannis, Y.C. Yortsos, Effect of liquid films on the drying of porous media, AIChE J. 50 (11) (2004) 2721–2737.
[31] A.G. Yiotis, D. Salin, E.S. Tajer, Y.C. Yortsos, Drying in porous media with gravity-stabilized fronts: experimental results, Phys. Rev. E - Stat. Nonlinear, Soft Matter Phys. 86 (2) (2012) 11–13.
[32] A.G. Yiotis, D. Salin, E.S. Tajer, Y.C. Yortsos, Analytical solutions of drying in porous media for gravity-stabilized fronts, Phys. Rev. E - Stat. Nonlinear, Soft Matter Phys. 85 (4) (2012) 1–12.
[33] M. Prat, On the influence of pore shape, contact angle and film flows on drying of capillary porous media, Int. J. Heat Mass Transf. 50 (7–8) (2007) 1455–1468.
[34] R.I. Al-Raoush, C.S. Willson, Extraction of physically realistic pore network properties from three-dimensional synchrotron X-ray microtomography images of unconsolidated porous media systems, J. Hydrol. 300 (1–4) (2005) 44–64.

[35] S. Beucher, F. Meyer, The morphological approach to segmentation: the watershed transformation, Optical Engineering vol. 34 (1992).
[36] T. Ransohoff, C. Radke, Laminar flow of a wetting liquid along the corners of a predominantly gas-occupied noncircular pore, J. Colloid Interface Sci. 121 (2) (1988) 392–401.
[37] D. Zhou, M. Blunt, F.M. Orr, Hydrocarbon drainage along corners of noncircular capillaries, J. Colloid Interface Sci. 187 (1) (1997) 11–21.
[38] H. Wong, S. Morris, C. Radke, Three-dimensional menisci in polygonal capillaries, J. Colloid Interface Sci. 148 (2) (1992) 317–336.
[39] G. Mason, N.R. Morrow, Meniscus curvatures in capillaries of uniform cross-section, J. Chem. Soc. Faraday Trans. 1 Phys. Chem. Condens. Phases 80 (9) (1984) 2375.
[40] R.P. Mayer, R.A. Stowe, Mercury porosimetry—breakthrough pressure for penetration between packed spheres", J. Colloid Sci. 20 (8) (1965) 893–911.
[41] H. Princen, Capillary phenomena in assemblies of parallel cylinders, J. Colloid Interface Sci. 30 (1) (1969) 69–75.
[42] P.-E. Oren, S. Bakke, O.J. Arntzen, Extending predictive capabilities to network models, SPE J. 3 (4) (1998) 324–336.
[43] J. Gostick et al., OpenPNM: a pore network modeling package, Comput. Sci. Eng. 18 (4) (2016) 60–74.
[44] L.A. Feldkamp, L.C. Davis, J.W. Kress, Practical cone-beam algorithm, J. Opt. Soc. Am. A 1 (6) (1984) 612–619.
[45] H. Dong, M. Blunt, Pore-network extraction from micro-computerized-tomography images, Phys. Rev. E 80 (3) (2009) 036307.
[46] D. Silin, T. Patzek, Pore space morphology analysis using maximal inscribed spheres, Phys. A Stat. Mech. its Appl. 371 (2) (2006) 336–360.
[47] S.P. Kuttanikkad, M. Prat, J. Pauchet, Pore-network simulations of two-phase flow in a thin porous layer of mixed wettability: application to water transport in gas diffusion layers of proton exchange membrane fuel cells, J. Power Sources 196 (3) (2011) 1145–1155.
[48] N. Neithalath, M.S. Sumanasooriya, O. Deo, Characterizing pore volume, sizes, and connectivity in pervious concretes for permeability prediction, Mater. Charact. 61 (8) (2010) 802–813.
[49] L.D. Poulikakos, M.N. Partl, A multi-scale fundamental investigation of moisture induced deterioration of porous asphalt concrete, Constr. Build. Mater. 36 (Nov.) (2012) 1025–1035.
[50] L.D. Poulikakos, A multi-scale fundamental investigation of moisture induced deterioration of porous asphalt concrete, ETH Zurich, 2011.
[51] T. Defraeye, B. Blocken, J. Carmeliet, Analysis of convective heat and mass transfer coefficients for convective drying of a porous flat plate by conjugate modelling, Int. J. Heat Mass Transf. 55 (2012) 112–124.
[52] N. Vorhauer, Y.J. Wang, A. Kharaghani, E. Tsotsas, M. Prat, Drying with formation of capillary rings in a model porous medium, Transp. Porous Media 110 (2) (2015) 197–223.